International Journal of Modern Physics C
Vol. 26, No. 1 (2015) 1550011 (17 pages)

DOI: 10.1142/S0129183115500114

World Scientific
www.worldscientific.com

Semi-automated scar detection in delayed enhanced cardiac magnetic resonance images

Rita Morisi

IMT Institute for Advanced Studies
Piazza S. Ponziano, 6, 55100, Lucca, Italy

Dipartimento di Fisica e Astronomia
Alma Mater Studiorum, University of Bologna
Viale Berti-Pichat 6/2, 40127 Bologna, Italy

Bruno Donini and Nico Lanconelli*

Dipartimento di Fisica e Astronomia
Alma Mater Studiorum, University of Bologna
Viale Berti-Pichat 6/2, 40127 Bologna, Italy
**nico.lanconelli@unibo.it*

James Rosengarden, John Morgan and Stephen Harden

University Hospital Southampton NHS Foundation Trust
Tremona Rd, Southampton SO16 6YD, UK

Nick Curzen

University Hospital Southampton NHS Foundation Trust
Tremona Rd, Southampton SO16 6YD, UK

Faculty of Medicine University of Southampton
Tremona Rd, Southampton SO16 6YD, UK

Received 3 April 2014
Accepted 26 May 2014
Published

Late enhancement cardiac magnetic resonance images (MRI) has the ability to precisely delineate myocardial scars. We present a semi-automated method for detecting scars in cardiac MRI. This model has the potential to improve routine clinical practice since quantification is not currently offered due to time constraints. A first segmentation step was developed for extracting the target regions for potential scar and determining pre-candidate objects. Pattern recognition methods are then applied to the segmented images in order to detect the position of the myocardial scar. The database of late gadolinium enhancement (LE) cardiac MR images consists of 111 blocks of images acquired from 63 patients at the University Hospital Southampton NHS Foundation Trust (UK). At least one scar was present for each patient, and all the scars were manually annotated by an expert. A group of images (around one third of the entire set) was used for training the system which was subsequently tested on all the remaining images. Four different classifiers were trained (Support Vector Machine (SVM), k-nearest neighbor (KNN),

Bayesian and feed-forward neural network) and their performance was evaluated by using Free response Receiver Operating Characteristic (FROC) analysis. Feature selection was implemented for analyzing the importance of the various features. The segmentation method proposed allowed the region affected by the scar to be extracted correctly in 96% of the blocks of images. The SVM was shown to be the best classifier for our task, and our system reached an overall sensitivity of 80% with less than 7 false positives per patient. The method we present provides an effective tool for detection of scars on cardiac MRI. This may be of value in clinical practice by permitting routine reporting of scar quantification.

Keywords: Image processing; computer aided detection; support vector machine.

PACS Nos.: 87.61.Tg, 87.85.dq.

1. Introduction

Magnetic Resonance Imaging (MRI) has long been used for imaging of the brain, spine and joints. Over the past decade, MRI has proven useful in diagnosing and improving the analysis of cardiovascular diseases. In particular, cardiac MRI is one of the emerging technologies in the noninvasive assessment of the function and structure of the cardiovascular system. Cardiac Magnetic Resonance (CMR) images provide clinicians with a detailed picture of the heart, and quantitative information about cardiac physiology can be derived directly from the images. Specifically, CMR allows quantitative assessment of functional parameters such as wall motion, wall thickness and ejection fraction.

The presence of scar tissue within the myocardium is clinically significant. For example fibrosis can be seen in disorders such as hypertrophic cardiomyopathy and infiltrative disorders, or secondary to ischemic injury where it indicates infarct. Furthermore, recent studies have indicated the existence of a clear relationship between myocardial scars and ventricular arrhythmia.[1–4] The presence of this kind of fibrotic tissue can act as a substrate for both tachy- and brady-arrhythmias.[5] In addition, the extent and distribution of scars may influence critical decisions in the clinical management of patients such as indications for revascularization, ablation for ventricular tachycardia and resynchronization therapy.[6] In this context, it could be useful to develop methods which were able to analyze left ventricle scars, in order to identify individuals at high risk of sudden cardiac death.

Late gadolinium Enhancement (LE) through CMR has emerged as the gold standard technique for the imaging of myocardial scars. In normal myocardium the concentration of gadolinium is low, whereas it increases in scar tissue, giving rise to hyper enhancement of affected areas. With respect to the surrounding living tissues, this appears as an area of high signal intensity.[5,7,8]

Current methods for the quantification of hyper enhancement images are slow and demand a lot of manual tracing across multiple slices. This requires both skill and time and it is therefore not done in routine clinical practice. This time-consuming task can be supported, simplified and accelerated by providing the clinicians with software which was able to analyze and collect parameters about heart function and

to determine the presence of myocardial scars. Software programs can also enable the measurement of a scar and peri-infarct zone by evaluating the signal intensity.

In this paper, we present a semi-automated method for detecting myocardial scars in CMR images. This algorithm is based on a model of scars comprising a set of features such as shape, size, brightness, contrast, etc. Scars are then isolated by using a classifier acting on the extracted features. The software is trained once with a suitable training set containing examples of lesions. Each example consists of an annotated image, with the description of the location and the contour of the scar. Once the location of the scars is indicated by our algorithm, this information can be used to help cardiologists in determining the position of the scar, or can be supplied as initial seed to a program that will realize a fine segmentation of the scars and the quantitative estimation of some important parameters.

2. Materials and Methods

A multi-step sequential flow consisting of three basic steps characterize the proposed method: extraction of the target region for potential scar, segmentation of all the objects located in that region and their final classification as *scar* or *no-scar*.[9] Our method is applied to all the 2D slices of each patient, one slice at a time.

2.1. *Database*

The database considered for training and testing our algorithm is composed of images acquired from 63 patients at the University Hospital Southampton NHS Foundation Trust (UK). All scans were performed with a dedicated 1.5–T Avanto MRI system (Siemens Medical Systems, Erlangen, Germany). Short-axis LE-CMR were acquired using a 3D segmented inversion recovery fast gradient echo sequence in two breath holds. For each breath hold, a block composed of usually 12 slices was acquired, giving rise to a total of 111 blocks. Most of the 2D slices have 256×200 pixels, with some exceptions, and the planar spatial resolution is 0.5 mm per pixel for the majority of cases, whereas the slice thickness is 4 mm. At least one left ventricular scar is present for all the patients. Each scar was manually annotated by a physician and the annotations were provided for all the slices containing the scar. Figure 1 shows an example of one block consisting of 12 slices which represents a portion of the left ventricle.

2.2. *Segmentation*

The purpose of the segmentation phase is to extract all the objects similar to scars that will be provided to the classifier. To this end, the proposed algorithm first determines the target region for potential scars. Subsequently, this region is segmented, and a series of signals is extracted and finally labeled.

First, the segmentation of the blood pool is realized through the use of a starting point provided by the user. This point must be positioned within the blood pool and

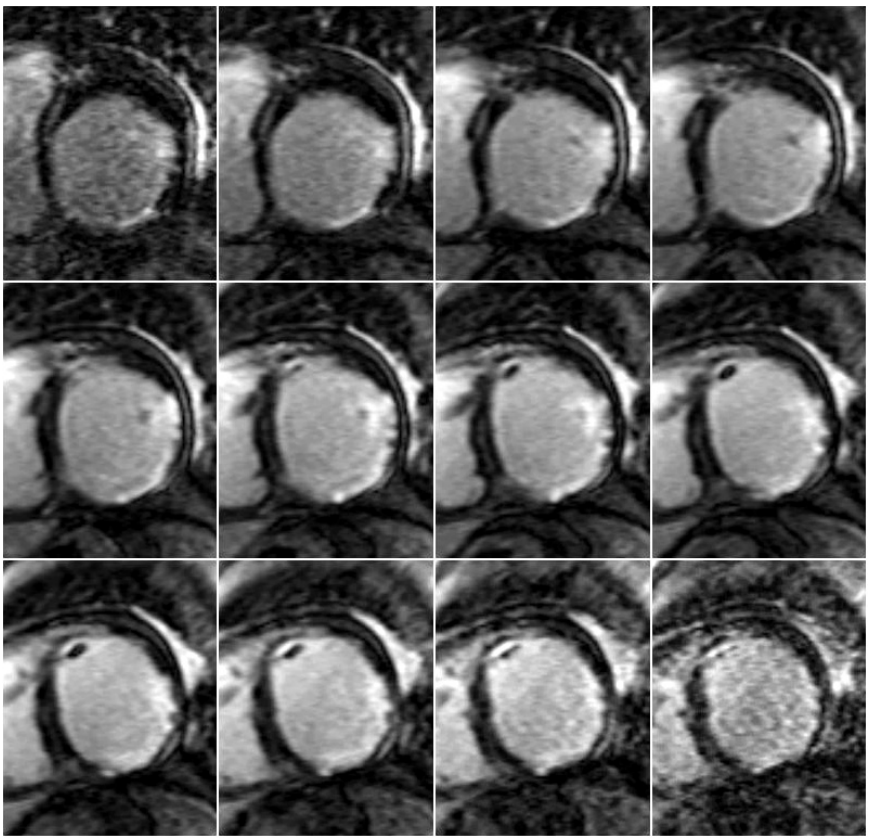

Fig. 1. LE-CMR study of a patient: in this case a block of 12 slices is shown, representing a portion of the left ventricle.

the user must indicate it for only one of the slices. Starting from this seed, the segmentation of the blood pool is realized by means of a 3D region growing algorithm: the region covered by the blood pool is thus extracted for all the slices.

We then make use of the segmented blood pool for determining the target region for potential scars. To this end, a curve indicating the position of the endocardium is estimated for each slice, through the following actions:

(1) Delineation of 16 different radial profiles on each slice, starting from the center of the blood pool.
(2) Computation of the average gray level (namely T) of the pixels inside the blood pool. For each profile, the position of the endocardium is estimated as the first pixel with a value lower than $\frac{T}{2}$, starting from the center of the blood pool. A graphical description of these first two steps is shown in Fig. 2. On the left is an example of a slice on which one of the 16 profiles is drawn, whereas the gray level of the pixels belonging to that profile is shown on the right.

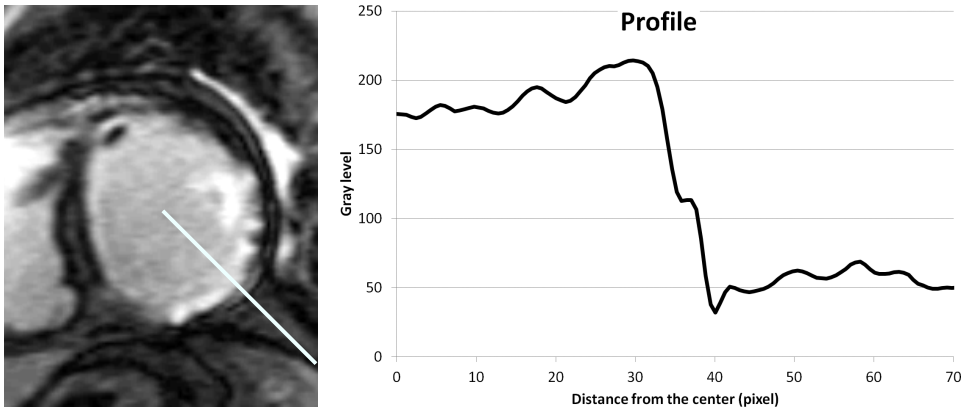

Fig. 2. Example of a profile which intersects the scar with the corresponding plot of the gray level distribution of the pixels (on the right). Moving from the center of the blood pool, it is possible to notice a remarkable drop in the profile, after approximately 35–40 pixels.

(3) Determination and solving of the critical situations: the absence of a pixel on a profile with a value lower than the threshold or the presence of a papillary muscle along the profile, which appears as a dark region within the blood pool. It can happen that no pixels along the profile present gray values lower than the threshold $\frac{T}{2}$. In this case, the position of the endocardium in that profile is determined as the largest one between the positions calculated for the two nearest profiles. In Fig. 3, we present an example where in some profiles there are no pixels with gray value below the threshold. The polygon passing through the 16 initial vertices is shown on the left, and the final polygon obtained by moving

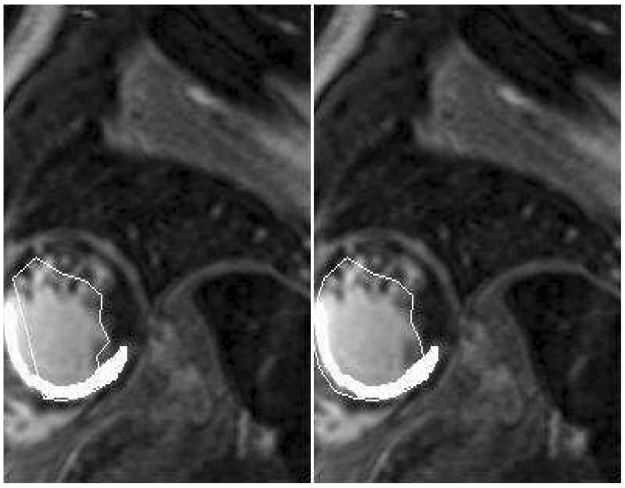

Fig. 3. Estimation of the polygon for determining the endocardium by using the method of the profiles before (left) and after (right) modifying the position of the critical vertices. The annotated scar (ground truth) is shown in white.

the position of some critical points is shown on the right. It is worth noting that a considerable portion of the scar (shown in white) is not included in the initial polygon, whereas the final corrected region includes the majority of the scar.

(4) Computation of an interpolating linear curve, as polygon passing through the vertices determined as described in (2) and (3). The interpolated curve represents our estimation of the endocardium.

(5) Determination of a circumference which represents the internal boundary of the region to be extracted. The radius of this circumference is estimated from the distance of the centroid of the polygon and the nearest vertex of the interpolated curve.

Once the target region is determined, an auto local threshold algorithm is applied on each image for extracting the brightest objects within that region. We chose Niblack's method,[10] in which each pixel belongs to the segmented objects only if its gray value is greater than $(\mu + Kt \cdot \sigma)$, where μ and σ are the average and the standard deviation of the gray distribution of the pixel's neighbors and Kt is the value of the threshold, respectively. The choice of Kt is important in preserving the shape of the segmented objects: it is essential to extract objects not too small and with a conformation similar to the shape of the scar.

2.3. *Scar classification*

The classification step aims to identify the segmented objects as *scar* or *no-scar*. To this end, a set of features were calculated for each signal and provided to a classifier. We considered 22 features, 12 related to the shape and geometry of the objects and 10 based on gray levels: 9 of the latter were computed by means of statistical descriptors of the gray distribution of the objects.

The first four gray level features were the *mean*, the *standard deviation*, the *kurtosis* and the *skewness*. Further four (e.g. energy, contrast, homogeneity and correlation) were statistical features connected to the image texture. These features were calculated according to the description reported in the literature and recently used in similar classification tasks.[11,12] In particular, we created the gray level co-occurrence matrices by using four directions (0°, 45°, 90° and 135°) and three distances (1, 3 and 5 pixels). Another feature considered is the entropy, which gives a statistical measure about the randomness of the distribution of the pixels. The last feature based on gray values is a measure of the contrast of the object, estimated as the difference between its average gray level and the average of its background.

The remaining 12 features based on the shape of the objects are:

(1) the *area* and the *perimeter* of the objects;
(2) the dimensions of the *bounding box*;
(3) the *major* and *minor axis* length and the *eccentricity* of the ellipse that has the same second central moment of the item;
(4) the *convex area* and the *solidity* related to the number of pixels of the minimal convex set that contains the connected points that make the object;

(5) the *Euler number*, related to the number of holes presented in a signal;
(6) the *equivalent diameter* of the circle with the same area of the region;
(7) the *scar rate*, which corresponds to the ratio between the areas of the object and the region defined by the segmentation step shown in the previous section.

We used the entire set of features for training and testing four different classifiers: a k-nearest neighbor (KNN), a neural network, a Bayesian classifier and a Support Vector Machine (SVM). In particular, we choose a feed-forward neural network with five hidden layers, while, for the KNN, we fix $k = 5$ and the Euclidean distance as the metric to evaluate the distance between the objects. We also used a quadratic Bayesian classifier with uncorrelated normal densities, and an SVM with polynomial kernel of second degree.

We then applied a feature selection algorithm to select the most important features, and potentially improve the generalization accuracy.[13] The evaluation function chosen to select the different characteristics is the Mahalanobis distance, used as metric to compute the distance between the two classes.[13]

2.4. *False positive reduction*

The goal of the final step is to reduce the number of false positive objects, rejecting signals classified as scars, by means of geometric considerations. Since the scars are located on the myocardium in the proximity of the blood pool, they are usually characterized by a curved shape with the convexity facing the blood pool. Given that some of the detected signals present an outward-facing convexity, we developed a method able to identify such signals. First, the skeleton of each signal is computed, and then the longest path which connects the vertices of the skeleton just determined is computed, by using the Dijkstra's algorithm.[14] The middle point of the path is then determined and its distance from the center of the blood pool (named d_1) is

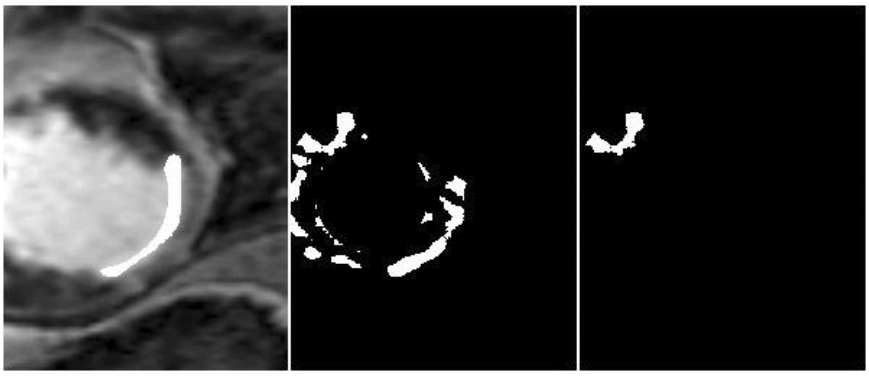

Fig. 4. Example of a signal with the convexity outward-facing rejected by our algorithm. Left: image with the scar shown in white. Center: results of the segmentation process. Right: object rejected by the false positive reduction step.

calculated. Finally, by comparing d_1 with the distance d_2 between the center of the blood pool and the segment with vertices the extremities of the skeleton, each signal with $d_2 > d_1$ is rejected, because it represents an object with an outward-facing convexity. Figure 4 shows an example of the false positive reduction (FPR) algorithm.

3. Results and Discussion

3.1. *Segmentation*

The segmentation process was developed and initially tested by using a small subset of the database: we used 30 blocks of images, less than 30% of the available database. Figure 5 shows some examples where the regions which can contain the scars are determined. The boundary of the endocardium is well approximated by the polygon drawn by using as vertices the points on the profiles. Anyway, the problem related to the presence of papillary muscles still occurs in some cases. For instance, in the 7th and 8th slice of the second block of images the papillary muscle inside (dark region in the upper-left part of the blood pool) is not included in the extracted endocardium, since in these slices the estimation of the point along the profile is positioned on the inner contour of the muscle. In general, it is quite difficult to model and adapt the curve in order to include these muscles inside the drawn curve. Different methods which make use of morphological connected operators (area-open and area-close filters) have been developed to solve this problem.[15,16] By evaluating the blocks of images presenting papillary muscles, in 74% of all cases our method is able to rearrange the polygon determining a more accurate conformation of the endocardium. Although the segmentation of CMR images is in general a challenging task, as stated elsewhere,[17] our algorithm is able to precisely delineate the endocardium inclusive of the scars in nearly all the cases. Indeed, in 96% of cases (i.e. patients) of the entire database, the segmentation step is able to determine a region which contains the scar in at least one slice per block. This means that the segmentation is responsible for only a 4% loss in the detection efficiency of the scars. After this first phase we applied the auto-local threshold algorithm to the determined region. The signals extracted from the images illustrated in Fig. 5 are presented in Fig. 6 (in white), together with the ground truth (in red). The data shown in Fig. 6 are obtained by using a Kt value of 0.6. It is worth noting that the items located on the same position of the scar preserve a conformation similar to the shape of the scarred tissue.

In order to choose the optimal auto-local threshold parameters, we made a first brief comparison between the results obtained with different Kt values by means of a visual assessment of the segmented objects. Figure 7 shows the 7th slice of the second patient presented in Figs. 5 and 6 and the segmented images obtained by applying the auto-local threshold method with a value of the threshold equal to 0.8 (second picture from the left), 0.45 (third from the left) and 0.6 (the last on the right). From this example, we can see that a Kt value of 0.8 creates small objects and the

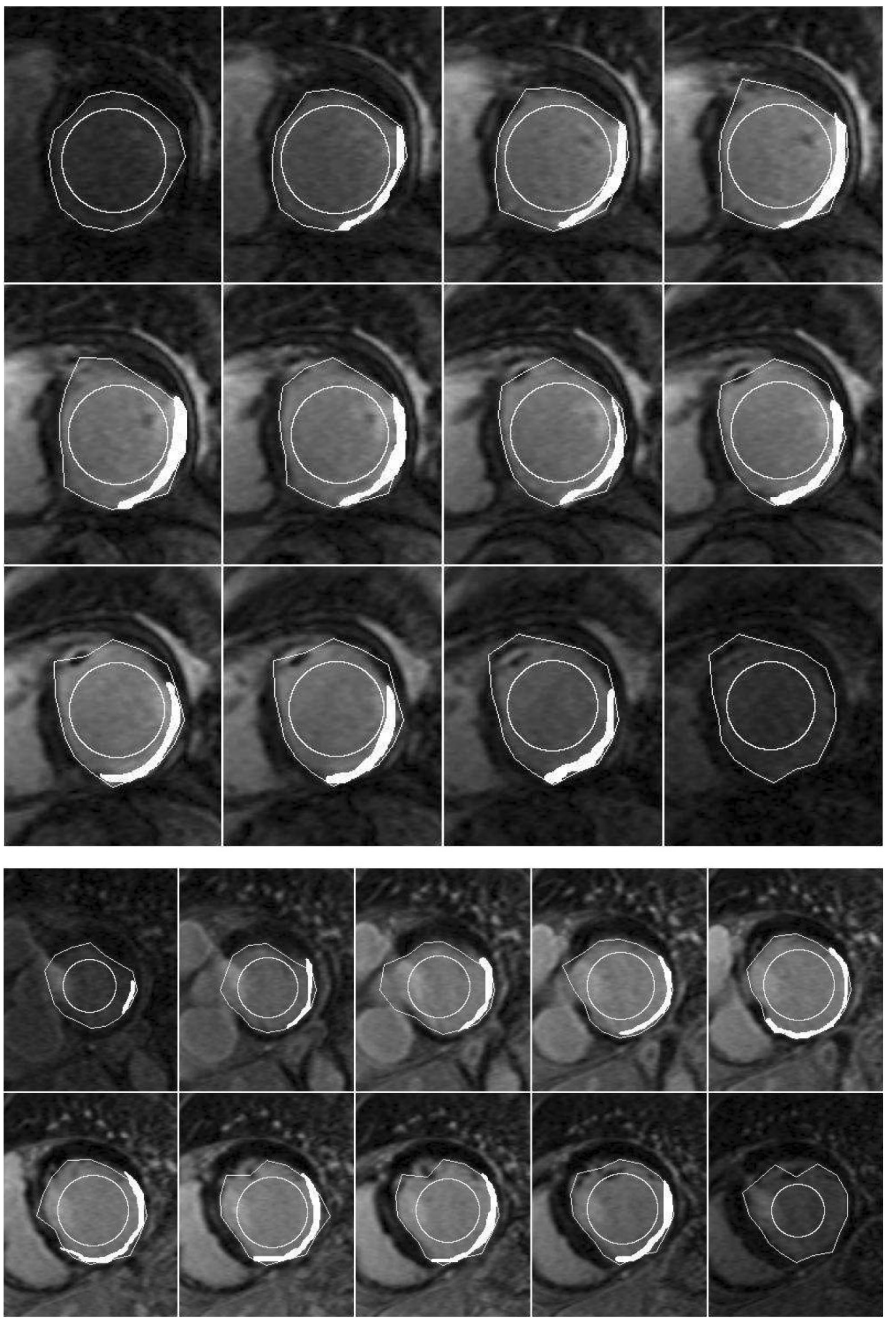

Fig. 5. Examples showing the extracted regions where the scar (shown in white) is supposed to be located. It is worth noting that the scar is always within the considered regions. The two blocks belong to two different patients.

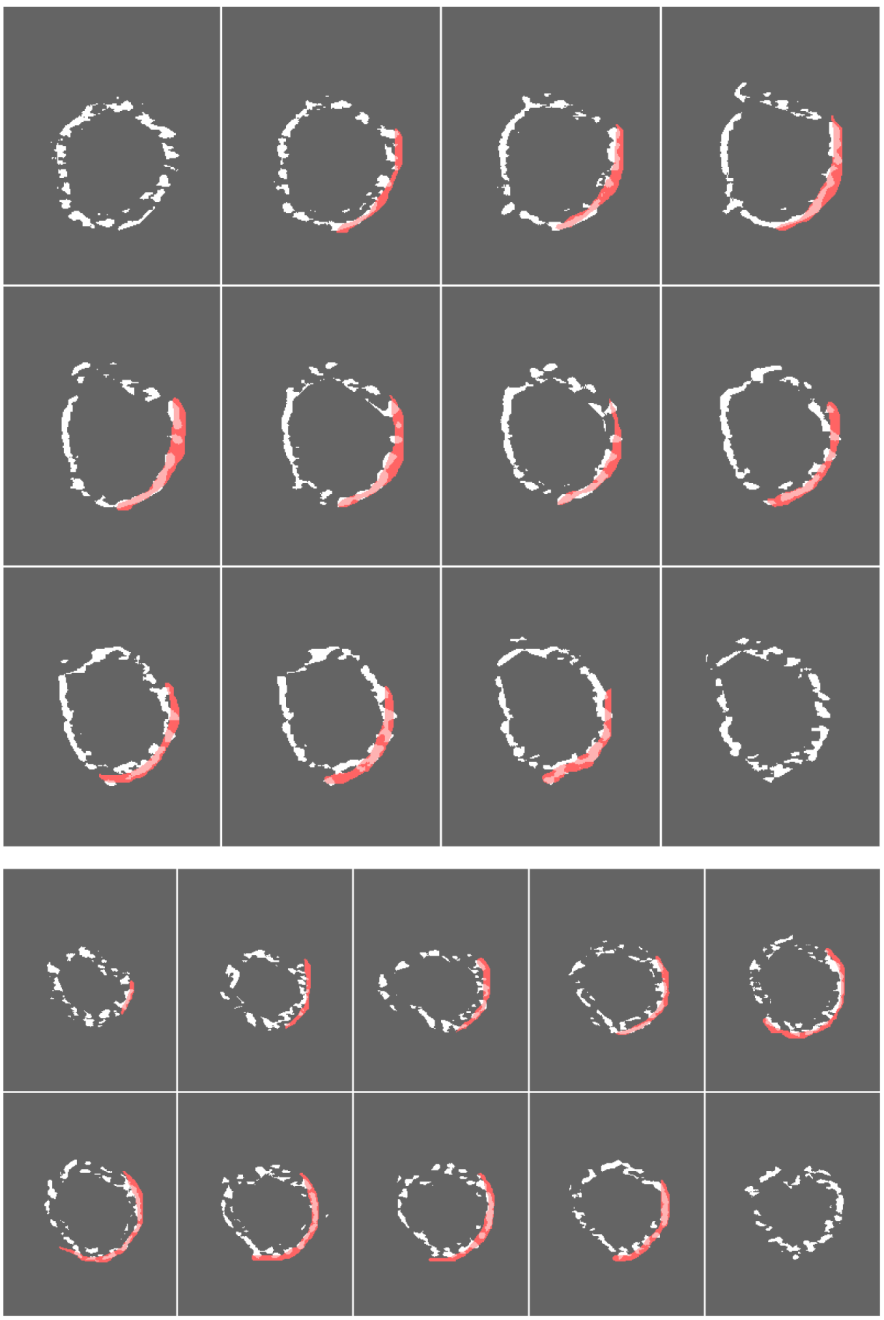

Fig. 6. (Color online) Signals segmented after the application of the auto-local threshold algorithm with $Kt = 0.6$ (shown in white). They are compared to the ground truth manually annotated by doctors, shown in red.

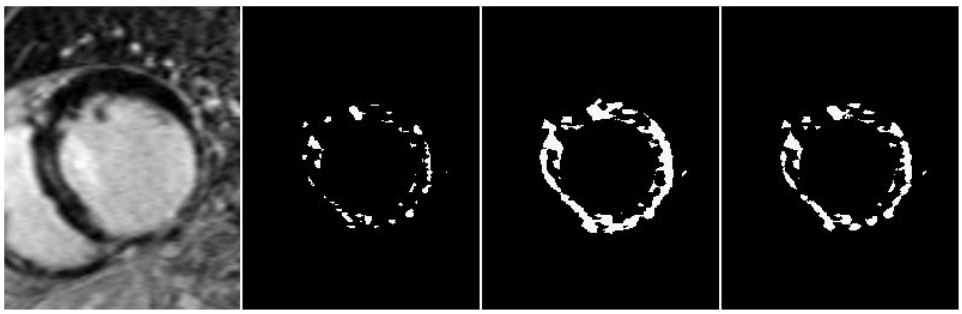

Fig. 7. Output comparison using three different values for Kt: 0.8 (second picture from the left), 0.45 (third from the left) and 0.6 (last picture on the right).

extracted signals can lose their peculiar shape, causing a more demanding subsequent pattern recognition task. Yet, setting the threshold parameter to 0.45 would generate a lower number of signals, since in general most of these are connected to each other. With these results a signal corresponding to the fibrosis could be too large and it may cause problems for the detection of the precise position of the scar. We believe that the Kt parameter set to 0.6 represents a valid tradeoff between the two situations. Furthermore, we will present in the next section a more accurate investigation of the Kt parameter after having applied the classifiers to the segmented objects. In that context, a further assessment will be made by analyzing the performance of the classifiers.

3.2. *Classification*

The entire database consisting of 111 blocks was used for training and testing the algorithm: 37 blocks for the training phase and the remaining 74 for the test. The training of each classifier was repeated five times, randomly selecting each time 37 blocks as training set and using the remaining 74 blocks for the test. We then averaged the results over the five testing groups, in order to give the average performance. The ground truth manually annotated by the clinicians was used to create the two classes (*scar* and *no-scar*) for the training set. To this end, the measure of the overlap between the scars and each segmented signal is computed for assigning all the signals of the training set to one of the two classes. The overlap is defined as the ratio between the intersection and the area of the smallest object between the two: if we denote by A_{GT} the area of the ground truth and by A_S the area of each signal, the overlap is then estimated as:

$$\mathrm{Overlap} = \begin{cases} \dfrac{A_{\mathrm{GT}} \cap A_S}{A_{\mathrm{GT}}} & \text{if } A_{\mathrm{GT}} < A_S, \\ \dfrac{A_{\mathrm{GT}} \cap A_S}{A_S} & \text{otherwise.} \end{cases} \tag{1}$$

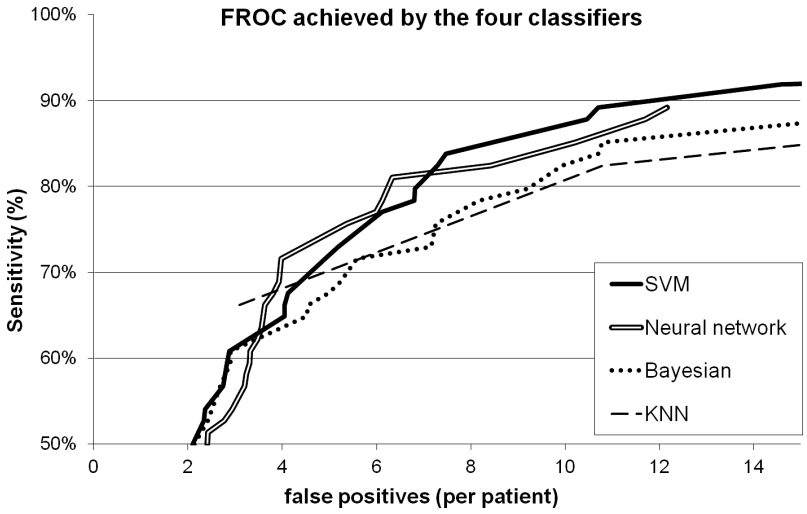

Fig. 8. FROC curves estimated on the test set for the four considered classifiers.

All the objects with an overlap with the scar greater than 40% are considered scars, while signals with an intersection less than 5% are labeled as no scar; all the other items are not considered in the training phase. In this way, the training set consists of 3800 signals, of which 15% are scars.

During the test, the output of the classifier was evaluated on a set composed of about 6500 signals. The objects classified as scar with an intersection with the ground truth greater than 20% are considered true positives, while the others are evaluated as false positives. The performances of the different classifiers were compared by means of Free response Receiver Operating Characteristic (FROC) curves. The sensitivity and the number of false positives are calculated on a *per block* basis (i.e. the false positives are reported as the average for the block and for each block a true positive is scored if in at least one slice a signal overlaps the scar with an intersection greater than 20%). The results obtained with the four classifiers using the entire set of 22 features and on the same training and test set are presented in Fig. 8. From this plot, it is clear that the SVM is able to provide the best outcomes.[18] We also checked the stability of the various classifiers with respect to their parameters and how their performance is affected by the size of the training set. Tables 1 and 2 show the outcomes of the four classifiers achieved after changing their parameters and the dimension of the training set, respectively. In this case, we evaluated the performances through the area under the FROC curve, estimated in the range between 2 and 15 false positives.

From Table 2, it is possible to infer that the neural network and the SVM are more sensitive than the other classifiers to the dimension of the training set. In addition, by changing the different probability distribution for the Bayesian classifier, the outcomes obtained with this system present remarkable differences: it

Table 1. Comparison between the areas under the FROC curves calculated by changing the parameters of the classifiers.

Classifiers	Parameter	Area
SVM	pol 1st degree	13.1 ± 0.1
	pol 2nd degree	14.2 ± 0.1
	homogeneous 2nd degree	13.9 ± 0.1
Neural network	1 hidden layer	12.2 ± 0.1
	3 hidden layers	12.3 ± 0.1
	5 hidden layers	13.5 ± 0.1
Bayesian classifier	uncorrelated	12.2 ± 0.1
	linear	8.1 ± 0.1
	quadratic	9.1 ± 0.1
KNN	5 neighbors	11.1 ± 0.1
	3 neighbors	10.2 ± 0.1
	9 neighbors	10.1 ± 0.1

Table 2. Comparison between the areas under the FROC curves calculated by changing the dimension of the training set.

Classifiers	1500 signals	2500 signals	Entire set
SVM	12.7 ± 0.1	13.4 ± 0.1	14.2 ± 0.1
Neural network	10.5 ± 0.1	12.8 ± 0.1	13.5 ± 0.1
Bayesian	12.1 ± 0.1	11.5 ± 0.1	12.2 ± 0.1
KNN	9.3 ± 0.1	11.8 ± 0.1	11.1 ± 0.1

reveals that it is very sensitive to the choice of its parameters. The uncorrelated Bayesian classifier achieves better results than the linear and the quadratic one. On the contrary, by changing the kernel function for the SVM similar results are achieved. Concerning KNN, Tables 1 and 2 reveal that this classifier is relatively stable and not very sensitive to changes in the parameters and dimension of the training set, but it provides worse results than those obtained with the SVM. We thus chose the SVM as classifier because of the best tradeoff achievable between its performance, stability, and dependence of the size of the training set, and we used this machine for the subsequent analysis.

We then realized a further investigation on the choice of the Kt parameters, after the visual assessment already achieved in the previous subsection. Table 3 and Fig. 9 show the results obtained with three different values of the Kt parameter: 0.45, 0.6 and 0.8. Although from Table 3, we can notice that the best performance is obtained by using $Kt = 0.45$, we decided to use the value 0.6 because the signals extracted with this threshold have a shape more suitable to represent the scars. From Fig. 9, it is clear that with $Kt = 0.45$, SVM labels as true positive a signal too large compared to the real scar, shown in red in the picture. This could create problems for the detection of the fibrosis, because in this way it could be difficult to find the exact

Table 3. Number of true positives (TP) and false positives (FP) detected by the SVM classifier on objects segmented with three different values of the Kt parameter.

TP	FP − $Kt = 0.8$	FP − $Kt = 0.45$	FP − $Kt = 0.6$
68%	3.5 ± 0.2	4.0 ± 0.2	4.1 ± 0.2
72%	4.5 ± 0.2	4.7 ± 0.2	4.9 ± 0.2
80%	6.5 ± 0.3	5.4 ± 0.2	6.8 ± 0.3
82%	10.2 ± 0.3	6.3 ± 0.3	7.3 ± 0.3
84%	10.5 ± 0.3	6.8 ± 0.3	7.5 ± 0.3

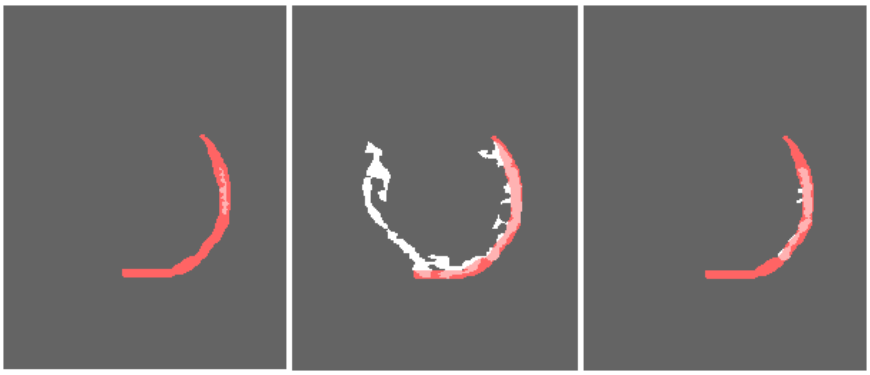

Fig. 9. (Color online) Outcomes obtained with the SVM applied to segmented images with different Kt parameters: 0.8 (left), 0.45 (middle) and 0.6 (right). The true annotation is shown in red.

position of the scar on the myocardium. Second, we also tested the output of the SVM by using a feature selection algorithm, in order to analyze the set of the considered features. Given that the dimension of the features space is not so high, we suspected that the application of a feature selection technique would not improve the performance of the classifier. However, such methods could be extremely useful in determining the most meaningful and important features of the entire set. By applying the features selection method to the entire set of characteristics, it turned out that 10 features are selected as the best ones. This subset is made up of 10 features, six describing the shape of the objects: the two dimensions of the bounding box, the perimeter and the area of the signal, the major axis length and the scar rate. The last four features are related to the gray distribution: the average gray level, the kurtosis, the homogeneity and the contrast of the object. Concerning the values related to the shape of the items, it is clear that some of them are irrelevant. For example, the three parameters of the ellipse with the same second central moment of the object give redundant information, because they are strictly related to each other. Only one of these values was chosen by the feature selection method. The performances achieved by the SVM with the entire set of features and the subset chosen by the feature selection method are presented in Fig. 10. It is worth noting that the outcomes

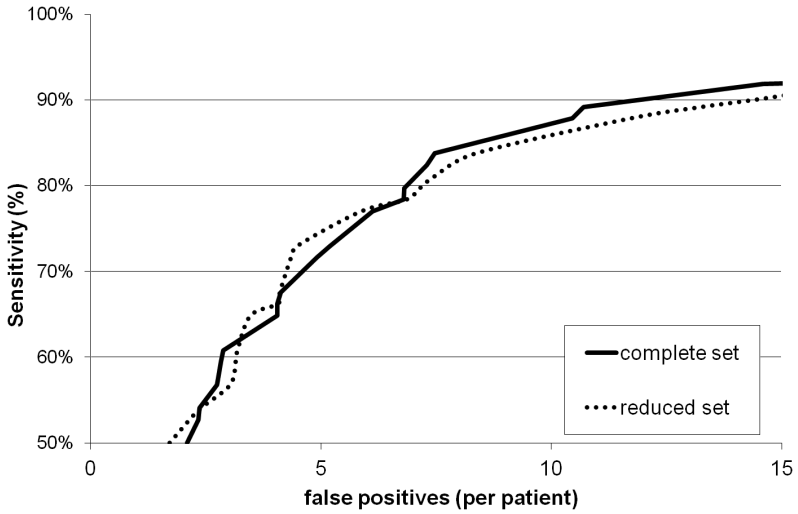

Fig. 10. Comparison of the performances of the SVM using the entire features set and a reduced set obtained with a features selection method. No clear advantage is noticeable in using the entire set of features.

obtained with the features subset do not change significantly. This means that with less than half features, the classifier is able to achieve a performance comparable to that obtained with all the characteristics. It is also true that for our study the feature selection algorithm does not improve the performance of the classifier, because our features set is relatively small and not particularly complex. Regardless, it was helpful to determine the minimal number of features that can guarantee similar performance of the classifier. This technique was then useful in eliminating redundant features and helped to get a better understanding of the most important ones.

Finally, we tested the efficacy of the FPR method, based on the determination of the outward-facing convexity of the objects labeled as scar by the SVM. The improvement on the performance of the classifier is shown in Table 4. It is worth noting that the FPR is able to slightly decrease the number of false positives, without losing any true positive.

Table 4. Number of true positives (TP) and false positives (FP) detected by our system before and after applying the FPR technique.

TP	FP before FPR	FP after FPR
66%	4.1 ± 0.2	3.9 ± 0.2
72%	4.9 ± 0.2	4.7 ± 0.2
77%	6.1 ± 0.2	5.9 ± 0.2
80%	6.8 ± 0.3	6.5 ± 0.3
84%	7.5 ± 0.3	7.2 ± 0.3
88%	10.5 ± 0.3	10.0 ± 0.3

By changing the final threshold of the classifier, it is possible to change the working point of the entire system (i.e. the sensitivity and the number of false positives). The choice of the most suitable working point is connected to how one decides to use the outcomes of the presented method. For instance, if the outcomes are going to be presented to a physician, probably it is better to produce outcomes with lower number of FPs, since a large number of false signals could disturb the viewing of the images. On the other hand, if we intend to use the outcomes as initial seed to a further program that will realize a refined segmentation of the scars, in this case it could be better to increase the efficiency.

4. Conclusions

In this paper, we presented a semi-automated method for myocardial scars detection applied to LE-CMR images. The segmentation step provides a 96% efficiency in including the scar inside the region extracted to be further analyzed. In other words, only in 4% of the blocks do we lose the possibility of detecting the scar in the first segmentation phase. It is worth noting that the segmentation phase is demanding also because of the quality of the images. Some are noisy, whilst in other cases the boundary of the myocardium is not well defined, or easily distinguishable. The analysis of various classifiers indicated that the best tradeoff, in terms of sensitivity, stability and dependence on the size of the training set was obtained with the SVM. With this classifier we reached an overall sensitivity of 80% with less than 7 false positives per patient. The feature selection method allowed us to halve the number of the initial features, without degrading the performance of the system. The analysis of the various features revealed which are the most important to be considered for the scar detection. Finally, the FPR method has demonstrated to be able to distinguish some false positives by evaluating their shape. In general, by applying this technique, the amount of false positives decreases by 0.5 false positives per block, keeping the same sensitivity.

While additional improvements are still needed, the method applied so far has already provided valuable and satisfactory results, which can lead to a significant step forward in the research on cardiac diseases. Further refinement of this method may lead to a tool that is valuable in routine clinical practice.

Acknowledgment

This work was supported by the EU-funded Project CHIRON (JU ARTEMIS Grant Agreement No. 100228).

References

1. F. M. Bogun, B. Desjardins, E. Good, S. Gupta, T. Crawford, H. Oral, M. Ebinger, F. Pelosi, A. Chugh, K. Jongnarangsin and F. Morady, *J. Am. Coll. Cardio.* **53**, 1138 (2009).

2. S. Nazarian, D. A. Bluemke, A. C. Lardo, M. M. Zviman, S. P. Watkins, T. L. Dickfeld, G. R. Meininger, A. Roguin, H. Calkins, G. F. Tomaselli, R. G. Weiss, R. D. Berger, J. A. Lima and H. R. Halperin, *Circulation* **112**, 2821 (2005).
3. P. A. Scott, J. M. Morgan, N. Carroll, D. C. Murday, P. R. Roberts, C. R. Peebles, S. P. Harden and N. P. Curzen, *Circ. Arrhythm Electrophysiol.* **4**, 324 (2011).
4. S. Mavrogeni, E. Petrou, G. Kolovou, G. Theodorakis and E. Iliodromitis, *Eur. Heart J. Cardiovasc. Imaging* **14**, 518 (2013).
5. C. J. Godeschalk-Slagboom, R. J. van der Geest, K. Zeppenfeld and C. P. Botha, *Int. J. Comput. Assist. Radiol. Surg.* **7**, 753 (2012).
6. T. D. Karamitsos and S. Neubauer, *Cardiovascular Magnetic Resonance*, eds. S. Redwood, N. Curzen and N. Thomas (Oxford Univesity Press, Oxford, 2010), p. 198.
7. N. M. I. Noble, D. L. G. Hill, M. Breeuwer and R. Razavi, *Lect. Notes Comput. Sci.* **3217**, 890 (2004).
8. R. M. Setser, D. G. Bexell, T. P. O'Donnell, A. E. Stillman, L. M. Lieber, P. Schoenhagen and R. D. White, *J. Magn. Reson. Imag.* **18**, 434 (2003).
9. S. Rampone, V. Pierro, L. Troiano and I. M. Pinto, *Int. J. Mod. Phys. C* **24**, 1350084 (2013).
10. W. Niblack, *An Introduction to Digital Image Processing* (Prentice Hall, Upper Saddle River, New Jersey, 1986), p. 115.
11. R. M. Haralick, K. Shanmugam and I. Dinstein, *IEEE Trans. Syst. Man Cybern.* **3**, 610 (1973).
12. C. Castella, K. Kinkel, M. P. Eckstein, P. E. Sottas, F. R. Verdun and F. O. Bochud, *Acad. Radiol.* **14**, 1486 (2007).
13. M. Dash and H. Liu, *Intell. Data Anal.* **1**, 131 (1997).
14. E. W. Dijkstra, *Numer. Math.* **1**, 269 (1959).
15. R. El Berbari, I. Bloch, A. Redheuil, E. D. Angelini, E. Mousseaux, F. Frouin and A. Herment, *Lect. Notes Comput. Sci.* **4466**, 453 (2007).
16. S. Huang, J. Liu, L. C. Lee, S. K. Venkatesh, L. L. Teo, C. Au and W. L. Nowinski, *J. Digit. Imaging* **24**, 598 (2011).
17. S. C. Mitchell, B. P. Lelieveldt, R. J. van der Geest, H. G. Bosch, J. H. Reiber and M. Sonka, *IEEE Trans. Med. Imaging* **20**, 415 (2001).
18. C. Z. Cai, W. L. Wang and Y. Z. Chen, *Int. J. Mod. Phys. C* **14**, 575 (2003).